Mahboubisarighieh *et al.*
Egypt J Radiol Nucl Med (2024) 55:118
https://doi.org/10.1186/s43055-024-01287-y

Egyptian Journal of Radiology and Nuclear Medicine

RESEARCH Open Access

Assessing the efficacy of 3D Dual-CycleGAN model for multi-contrast MRI synthesis

Ali Mahboubisarighieh[1], Hossein Shahverdi[2], Shabnam Jafarpoor Nesheli[3], Mohammad Alipoor Kermani[4], Milad Niknam[5], Mohanna Torkashvand[6] and Seyed Masoud Rezaeijo[7*]

Abstract

Background This research presents a novel methodology for synthesizing 3D multi-contrast MRI images utilizing the 3D Dual-CycleGAN architecture. The performance of the model is evaluated on different MRI sequences, including T1-weighted (T1W), T1-weighted contrast-enhanced (T1c), T2-weighted (T2W), and FLAIR sequences.

Results Our approach demonstrates proficient learning capabilities in transforming T1W images into target modalities. The proposed framework encompasses a combination of different loss functions including voxel-wise, gradient difference, perceptual, and structural similarity losses. These loss components, along with adversarial and dual cycle-consistency losses, contribute significantly to realistic and accurate syntheses. Evaluation metrics including MAE, PMAE, RMSE, PCC, PSNR, and SSIM are employed to assess the fidelity of synthesized images compared to their ground truth counterparts. Empirical results indicate the effectiveness of the 3D Dual-CycleGAN model in generating T1c images from T1W inputs with minimal average discrepancies (MAE of 2.8 ± 2.61) and strong similarity (SSIM of 0.82 ± 0.28). Furthermore, the synthesis of T2W and FLAIR images yields promising outcomes, demonstrating acceptable average discrepancies (MAE of 3.87 ± 3.32 for T2W and 3.82 ± 3.32 for FLAIR) and reasonable similarities (SSIM of 0.82 ± 0.28 for T2W and 0.80 ± 0.29 for FLAIR) relative to the original images.

Conclusions These findings underscore the efficacy of the 3D Dual-CycleGAN model in generating high-fidelity images, with significant implications for diverse applications in the field of medical imaging.

Keywords Generating, MRI, 3D multi-contrast MRI, 3D Dual-CycleGAN

Background

Magnetic resonance imaging (MRI) has become widely utilized in clinical diagnosis and treatment. It is a popular imaging technique alongside computed tomography (CT), type-B ultrasonic (B-scan), and positron emission tomography (PET). MRI stands out from these methods due to its non-invasive nature, and similarly, ultrasound is also non-invasive [1]. By employing various pulse sequences and parameters, MRI can generate distinct tissue contrasts, resulting in different modalities of the same anatomical structure [2]. Each sequence of MRI possesses unique anatomical characteristics that provide supplementary information and enhance diagnostic capabilities in conjunction with other modalities. Commonly acquired modalities include T1-weighted (T1W), T2-weighted (T2W),

*Correspondence:
Seyed Masoud Rezaeijo
rezaei-sm@ajums.ac.ir
[1] Department of Computer Engineering, University of Kharazmi, Tehran, Iran
[2] Department of Electrical Engineering, University of Shahid Beheshti, Tehran, Iran
[3] Faculty of Engineering, University of Science and Culture, Tehran, Iran
[4] Department of Computer Engineering, University of Shahid Bahonar, Kerman, Iran
[5] Department of Computer Engineering, Islamic Azad University, Nurabad Mamasani, Iran
[6] Department of Computer Engineering, Hamedan University of Technology, Hamedan, Iran
[7] Department of Medical Physics, Faculty of Medicine, Ahvaz Jundishapur University of Medical Sciences, Ahvaz, Iran

T1-with-contrast-enhanced (T1c), and T2-fluid-attenuated inversion recovery (FLAIR). Each sequence exhibits specific pathological features, and the integration of multiple modalities, known as multi-modal MRI, can further enrich diagnostic information for healthcare professionals. However, practical considerations, such as the cost of lengthy examinations or uncooperative patients, particularly in the pediatric and elderly populations, may make it impractical to acquire a complete range of contrasts [3, 4]. In such cases, acquiring contrasts with shorter scan times may be preferred. Conversely, shortening the acquisition time can result in decreased image quality [5, 6]. Additionally, excessive noise and metal artifacts can hinder the acquisition of complete sequences. The loss of certain MRI sequences can lead to an increase in diagnostic inaccuracies. To overcome these challenges and address the limitations, the utilization of image synthesis methods can be employed.

Image synthesis, a technique used to transform given images into a specific type, has found extensive applications in the medical field [7–10]. Over the past few decades, several methods have been proposed to synthesize the required target MRI sequence using single-sequence input [11–14]. However, these methods have limitations in capturing comprehensive features and pathological information. On the other hand, the unique information from different MRI modalities complements each other [15]. Consequently, there has been a growing interest in multi-modal MRI image synthesis, which aims to enhance the quality of synthetic images and improve diagnostic utility [16–21]. Recent advancements have introduced methods that enable training with unregistered or unpaired data. State-of-the-art techniques often employ deep convolutional neural networks (CNN) as the image generator within a generative adversarial network (GAN) framework [22]. GANs offer the ability to represent sharp and complex probability densities through a nonparametric approach [23–25]. They have been widely adopted in medical image analysis, particularly for tasks like data augmentation and multi-sequence image translations, due to their capability to handle domain shift [26–28]. To address the issue of domain-specific deformations being encoded as domain-specific features and reproduced in the synthesized output, researchers have integrated CycleGAN into the training process. Previous studies have demonstrated that CycleGAN can be trained using unpaired brain data [29]. However, these studies were more limited to training the network on a single slice and were two-dimensional in nature [8, 29, 30]. Moreover, image synthesis was primarily performed within a single modality, such as synthesizing T1W from T2W or synthesizing T2W from FLAIR and vice versa. This study aims to synthesize 3D Multi-Contrast MRI using 3D Dual-CycleGAN.

Methods

Dataset

The MRI data utilized were collected from the Multimodal Brain Tumour Segmentation Challenge (BraTS) 2021 [22, 31–34]. The training dataset of BraTS 2021 comprised 1251 MR volumes, each with dimensions of $240 \times 240 \times 155$. MRI scans play a crucial role in evaluating tumor heterogeneity. Specifically, the following MRI sequences conventionally employed in glioma detection were included: T1W, T1c, T2W, and FLAIR sequences. T1W images are excellent for anatomical detail, as they highlight differences in tissue density. In brain imaging, T1W images typically depict gray matter as dark and white matter as bright. T1c images are particularly useful for highlighting regions of abnormal vascularity, such as tumors. Gadolinium-based contrast agents enhance areas with disrupted blood–brain barriers, aiding in the detection and characterization of lesions. T2W images highlight differences in water content and are valuable for detecting abnormalities like edema, inflammation, and cerebrospinal fluid. In brain imaging, cerebrospinal fluid appears bright, while white matter appears darker than on T1W images. FLAIR sequences suppress the signal from cerebrospinal fluid, enhancing the visibility of pathological tissues while reducing CSF artifacts. This makes FLAIR particularly useful for detecting lesions adjacent to cerebrospinal fluid spaces, such as multiple sclerosis plaques and small tumors. These sequences enable the identification of four distinct tumor sub-regions on MRI scans: the Enhancing Tumor (ET) characterized by relative hyper-intensity in the T1c sequence compared to the T1 sequence, the Non-Enhancing Tumor (NET), the Necrotic Tumor (NCR) which both exhibit hypointensity in T1c relative to T1 and the Peritumoral Edema (ED) displaying hyper-intensity in the FLAIR sequence. Figure 1 displays the MRI sequences along with the ground truth map.

Overview of proposed method

In this section, we present a comprehensive overview of our proposed method for MR image synthesis. Our approach leverages cutting-edge techniques such as 3D Dual-CycleGAN model to generate T1c, T2W, and FLAIR-like images from T1W images. The process begins by employing a 3D Dual-CycleGAN model, which learns the mapping between T1W images and the target modalities (T1c, T2W, and FLAIR). This model enables the transformation of T1W images into the desired modalities, capturing the specific characteristics and information unique to each modality. This model focuses on

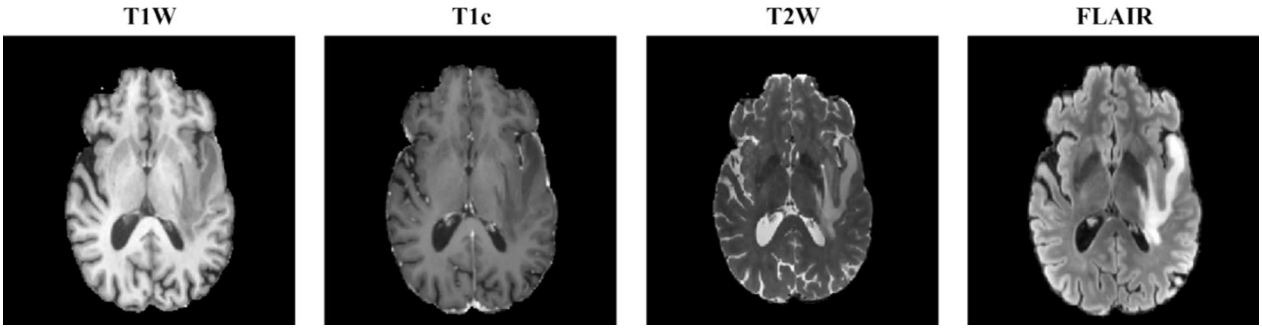

Fig. 1 Visualization of the BraTS 2021 training data analysis

enhancing the fine details, textures, and overall quality of the generated images, resulting in more realistic and visually appealing representations. The generated images offer a comprehensive and accurate depiction of the target modalities, allowing for a deeper understanding of the underlying structures and pathology. In the subsequent sections, we will discuss the evaluation metrics employed to assess the similarity between the synthesized images and the original images, providing a quantitative measure of the effectiveness and fidelity of our proposed methods.

3D Dual-CycleGAN

The CycleGAN introduces a revolutionary and sophisticated solution to address the challenge of unpaired image-to-image translations. In contrast to traditional supervised methods that require a direct one-to-one correspondence between images in the dataset, the CycleGAN leverages a cycle consistency loss to enable image translation using unpaired datasets. This architecture is comprised of two generators and two discriminators. The primary generator takes an image X and transforms it into an image Y, while the secondary generator performs the opposite function by converting a Y image into an X image. The discriminators serve as judges to determine the authenticity of the generated images. The X image discriminator assesses whether the generated X image faithfully represents the original X, and similarly, the Y image discriminator evaluates the fidelity of the generated Y image to the original Y. Each generator and discriminator has its own distinct loss functions tailored to their roles. Notably, the cycle consistency loss assumes a pivotal role within this architecture. It ensures that the translated X image closely resembles the original Y image in terms of pixel-level details, and conversely, the translated Y image accurately captures the essence of the original X image.. The overall loss function for the CycleGAN encompasses both the adversarial loss and the cycle consistency loss. The adversarial loss (LGAN) gauges the performance of the generator and discriminator, while the cycle consistency loss (Lcyc) quantifies the similarity between the original and translated images. The objective of this architecture is to minimize the aggregate loss (L), which is a combination of LGAN, Lcyc, and a parameter λ. During the generator's training process, the output image is passed through the other generator to reconstruct the input image.

The 3D Dual-CycleGAN model is a learning technique that combines supervised and unsupervised training methods. It uses a small portion of aligned data for supervised learning and a large amount of unaligned data for unsupervised learning. This approach allows for a larger number of images to be used during training, resulting in a more stable model. Moreover, the combination of supervised and unsupervised learning helps reduce model bias and improve generalization. The 3D Dual-CycleGAN consists of two CycleGAN networks, which are trained using shared weights and both supervised and unsupervised learning methods. To achieve accurate and visually pleasing outputs, four loss functions are utilized: voxel-wise, gradient difference, perceptual, and structural similarity losses. These four terms, along with the adversarial and dual cycle-consistency losses, are combined to create the overall loss function, denoted as Lsup = Lsup-adversarial + Lsup-cycle-consistency + Lvoxel-wise + Lgradient + Lperceptual + Lstructural. The mappings used for generating T1c, T2W, and FLAIR images from T1W. In this study, the Generative T1W (Gen T1W) network is designed to synthesize images that resemble those in the T1c, T2W, and FLAIR domains. On the other hand, the Discriminative T1c, T2W, and FLAIR (Dis T1c, T2W, and FLAIR) network aims to distinguish between real and synthetic T1c, T2W, and FLAIR images. Two types of adversarial loss equations are used to evaluate the performance of these networks: a supervised adversarial loss equation ($L_{sup\text{-}adver}$) and an unsupervised adversarial loss equation ($L_{unsup\text{-}adver}$). In addition to the adversarial loss, a dual cycle-consistent structure ($L_{sup\text{-}cycle}$ and $L_{unsup\text{-}cycle}$) is

employed to minimize the gap between the low and high b-value domains.

The 3D Dual-CycleGAN model, which incorporates both forward and backward adversarial losses, is illustrated in Fig. 2. Additionally, Fig. 3 presents a visual representation of the network structure of this model.

Implementation

In this study, we utilized 3D Dual CycleGAN to generate T1c, T2W, and FLAIR images from T1W images. The optimization of parameters involved the consideration of six distinct loss terms, carefully balancing quantitative and qualitative aspects. These loss terms included adversarial, dual cycle-consistent, voxel-wise, gradient difference, perceptual, and structural similarity losses. The default initialization parameters were employed for this purpose. The training of the networks spanned 4000 epochs, conducted with a batch size of 8. The dataset used in the study was split into two subsets: a training set consisting of 1000 samples and a testing set comprising 251 samples. To facilitate a comprehensive comparison between real and synthetic images, we employed five well-established metrics, elaborated upon in "Appendix". These metrics encompassed Mean Absolute Error (MAE), Percent Mean Absolute Error (PMAE), Root Mean Squared Error (RMSE), Pearson Correlation Coefficient (PCC), Peak-Signal-to-Noise Ratio (PSNR), and Structural Similarity Index Measure (SSIM). These metrics are commonly employed within the medical image evaluation domain.

Results

The present study utilized the 3D Dual CycleGAN deep learning algorithm to synthesize T1c, T2W, and FLAIR images from T1W inputs. The performance of the model was evaluated by comparing the generated images with the original ones, and the results for each image type are as follows:

T1c image synthesis

The 3D Dual CycleGAN demonstrated excellent performance in generating T1c images from T1W inputs. The MAE was measured at 2.8 ± 2.61, indicating a relatively small average discrepancy between the original and synthesized images. The RMSE was calculated as 7.96 ± 5.2, implying a slightly larger overall error. However, these values were within an acceptable range considering the complexity of the task. The SSIM showed a high similarity of 0.82 ± 0.28 between the original and synthesized images, further affirming the accuracy of

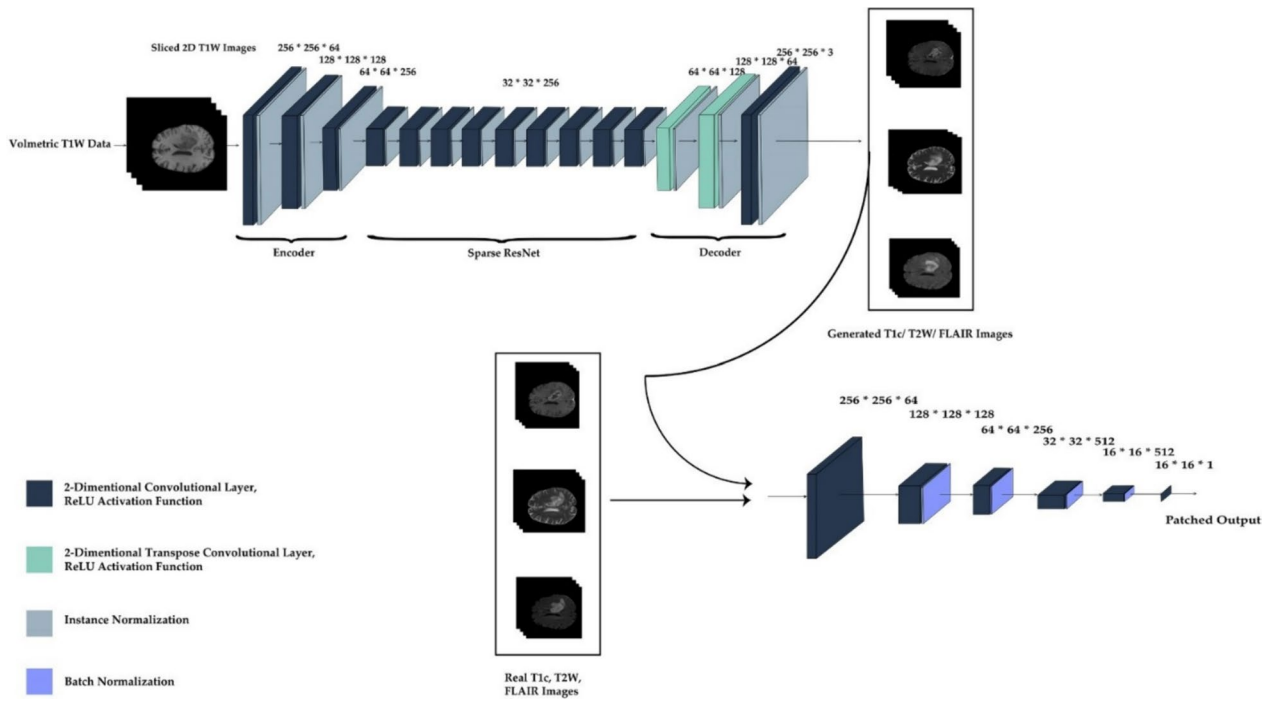

Fig. 2 The architecture of the 3D Dual-CycleGAN model for T1W to T1c, T2W, and FLAIR image transition. The figure illustrates the structure of the Dual-CycleGAN model, which is composed of two separate CycleGAN. The model incorporates four different loss functions: voxel-wise, gradient difference, perceptual, and structural similarity losses. Both the Generator and Discriminator networks are utilized in the models to facilitate the transformation from T1W images to T1c, T2W, and FLAIR images

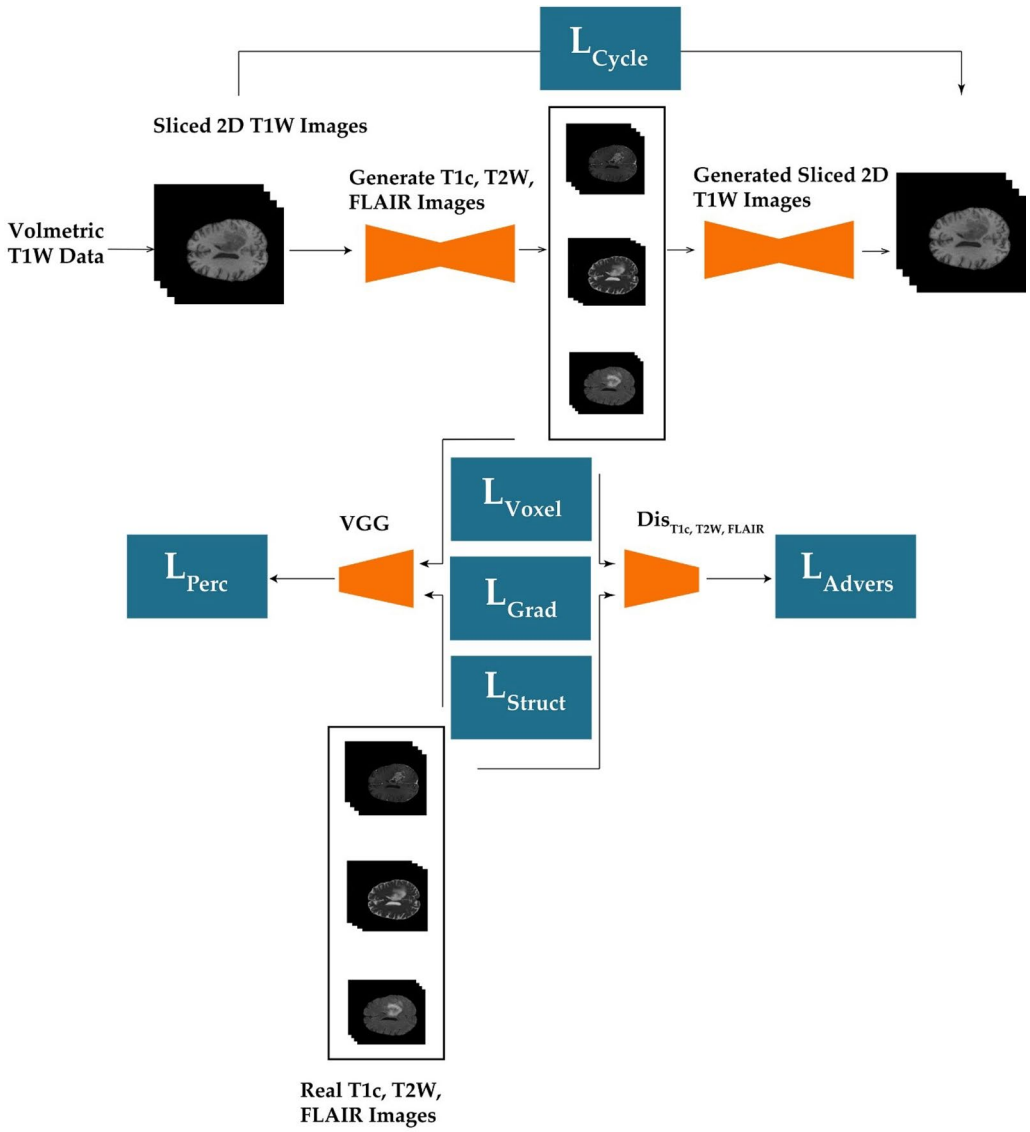

Fig. 3 Architecture of the Dual-CycleGAN model, based on two CycleGAN. Four loss functions were employed: voxel-wise, gradient difference, perceptual, and structural similarity losses

the generated T1c images. Additionally, the PCC measured at 0.84 ± 0.29 indicated a strong linear relationship between the original and synthesized images. The PSNR was evaluated as 84.55 ± 18.19, reflecting a high level of fidelity in the generated T1c images.

T2W image synthesis

The synthesis of T2W images from T1W inputs yielded satisfactory results using the 3D Dual CycleGAN. The MAE was calculated as 3.87 ± 3.32, indicating a slightly higher average discrepancy compared to T1c synthesis. The RMSE measured at 11.04 ± 6.78 indicated a relatively larger overall error. However, the SSIM of 0.82 ± 0.28 still indicated a considerable similarity between the original and synthesized T2W images. The PCC value of 0.83 ± 0.29 suggested a strong linear relationship between the two image types. The PSNR was evaluated as 67.5 ± 23.68, implying a slightly lower level of fidelity compared to T1c synthesis but still within an acceptable range.

FLAIR image synthesis

The synthesis of FLAIR images from T1W inputs using the 3D Dual CycleGAN also yielded promising results. The MAE was measured at 3.82 ± 3.32, slightly higher than T1c synthesis but still within an acceptable range.

The RMSE calculated as 10.02 ± 6.45 indicated a moderate overall error. The SSIM of 0.80 ± 0.29 indicated a reasonable similarity between the original and synthesized FLAIR images. The PCC value of 0.84 ± 0.30 suggested a strong linear relationship between the two image types. The PSNR was evaluated as 81.63 ± 15.49, indicating a high level of fidelity in the generated FLAIR images. In summary, the results demonstrate that the 3D Dual CycleGAN model effectively synthesizes T1c, T2W, and FLAIR images from T1W inputs. While the accuracy and fidelity varied slightly across the three image types, all generated images exhibited a substantial resemblance to the original images. These findings highlight the potential of the 3D Dual CycleGAN algorithm in enhancing the synthesis of multi-contrast MRI images, contributing to improved diagnostic accuracy and aiding in the identification of glioma tumors. In order to quantitatively compare the synthetic images generated using 3D Dual CycleGAN, we present box plots in Fig. 4 that illustrate the MAE, RMSE, PSNR, SSIM, and PCC. Each box plot is accompanied by circles representing individual image slices from the test dataset. The upper and lower limits of the box plot were determined using the 25th and 75th percentiles (Q25 and Q75, respectively). The average and median are indicated by green triangles and horizontal lines, respectively. The range of the whiskers in the box plot is defined as $[Q25 - 1.5 \times (Q75 - Q25), Q75 + 1.5 \times (Q75 - Q25)]$.

Figure 5a showcases a comprehensive evaluation of various image types, including real T1W, real T1c, synthesized T1c, and absolute difference maps depicting disparities between the synthesized and real T1c images. Similarly, Fig. 5b provides an in-depth analysis of real T1W, real T2W, synthesized T2W, and absolute difference maps highlighting dissimilarities between the synthesized and real T2W images. Additionally, Fig. 5c presents a detailed examination of real T1W, FLAIR, synthesized FLAIR, and absolute difference maps accentuating variations between the synthesized and real FLAIR images. It is worth noting that each condition of the synthetic images is thoughtfully represented by four carefully selected image slices. The robust implementation of the 3D Dual CycleGAN architecture effectively ensures the preservation of essential characteristics such as coherence and smoothness in the synthesized images. Notably, the synthesized MR images, regardless of contrast variations, exhibit an impressive resemblance to their corresponding real counterparts. This striking similarity can be attributed to the integration of cycle-consistent networks, which allow for the acquisition of knowledge from unpaired data. Through this iterative process, the synthesized images achieve an exceptional level of fidelity, rendering them virtually indistinguishable from the real images even by highly experienced medical professionals during our meticulous validation procedures.

Discussion

The utilization of medical imaging techniques that capture the same anatomical structure yet exhibit varying contrasts significantly broadens the scope of diagnostic information. However, certain challenges, such as prolonged scanning durations, can impede the accurate delineation of specific contrasts, which might be further compromised by the presence of noise and artifacts. In such situations, the ability to generate missing or deteriorated contrasts becomes pivotal to optimize diagnostic efficacy. In this investigation, we harnessed the power of the 3D Dual CycleGAN deep learning algorithm to create T1c, T2W, and FLAIR images through the transformation of T1W images. The outcomes attained underscore the robustness of the 3D Dual CycleGAN model in effectively producing these synthesized images from T1W inputs. Our findings vividly illustrate the potential of this algorithm in elevating the process of synthesizing multi-contrast MRI images.

In comparison to the research conducted by Xie et al. [35], their work introduced a technique centered on generating high-resolution (HR) magnetic resonance (MR) images from low-resolution MR images through the utilization of a parallel CycleGAN framework. Although the objectives of their study varied, both investigations underscore the effectiveness of CycleGAN-based methodologies in producing realistic medical image reconstructions. While Xie et al.'s investigation [35] aimed to expedite the MR image acquisition process, our research concentrated on the synthesis of 3D multi-contrast MRI images to enhance the accuracy of tumor identification. Notably, the evaluation metrics employed differ, posing challenges in establishing direct quantitative comparisons. Nevertheless, both studies vividly exemplify the potential inherent in leveraging deep learning algorithms to augment the synthesis of MR images.

Another relevant study by Xie et al. [36] aimed to derive synthetic contrast-enhanced MR images from unenhanced images, eliminating the need for gadolinium-based contrast agents (GBCAs). They utilized a cascade deep learning workflow that incorporated contour information into the network. For the hold-out test patients, the average values and standard deviations of the Normalized NMAE, SSIM, and PCC were calculated. In the entire brain, the mean NMAE was 0.063 with a standard deviation of 0.022, the mean SSIM was 0.991 with a standard deviation of 0.007, and the mean PCC was 0.995 with a standard deviation of 0.006. In the tumor contour regions, the mean NMAE was 0.050 with a standard deviation of 0.025, the mean SSIM was

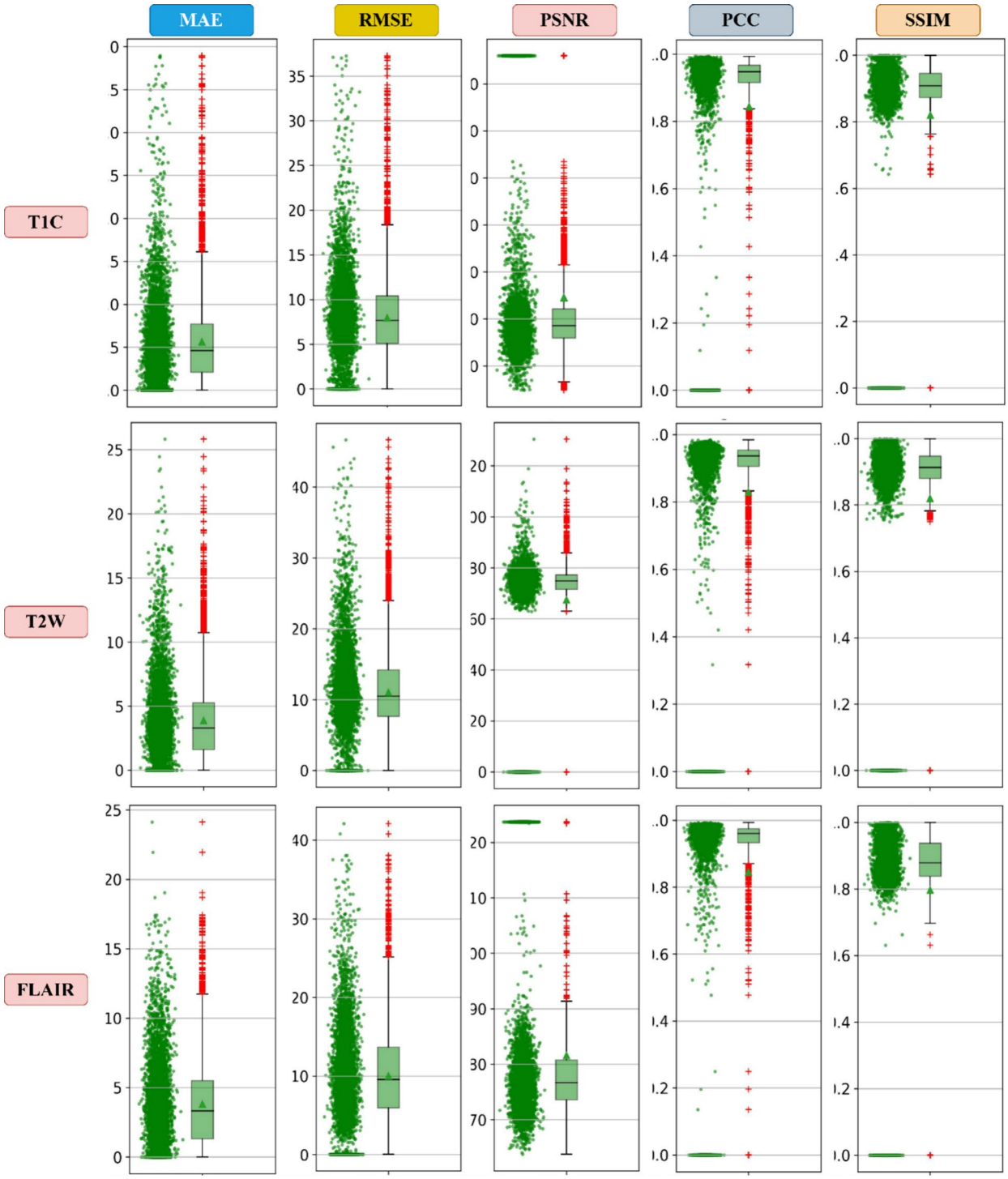

Fig. 4 A comparison of the proposed approach is depicted based on the following metrics: MAE, RMSE, PSNR, SSIM, and PCC

0.993 with a standard deviation of 0.008, and the mean PCC was 0.999 with a standard deviation of 0.003. Although the objectives of their study differ from ours, as they focused on contrast enhancement, it is interesting to note that both studies leverage deep learning techniques to enhance the quality of MR images. Our study contributes to the field by successfully synthesizing T1c, T2W, and FLAIR images from T1W inputs, improving the identification of glioma tumors.

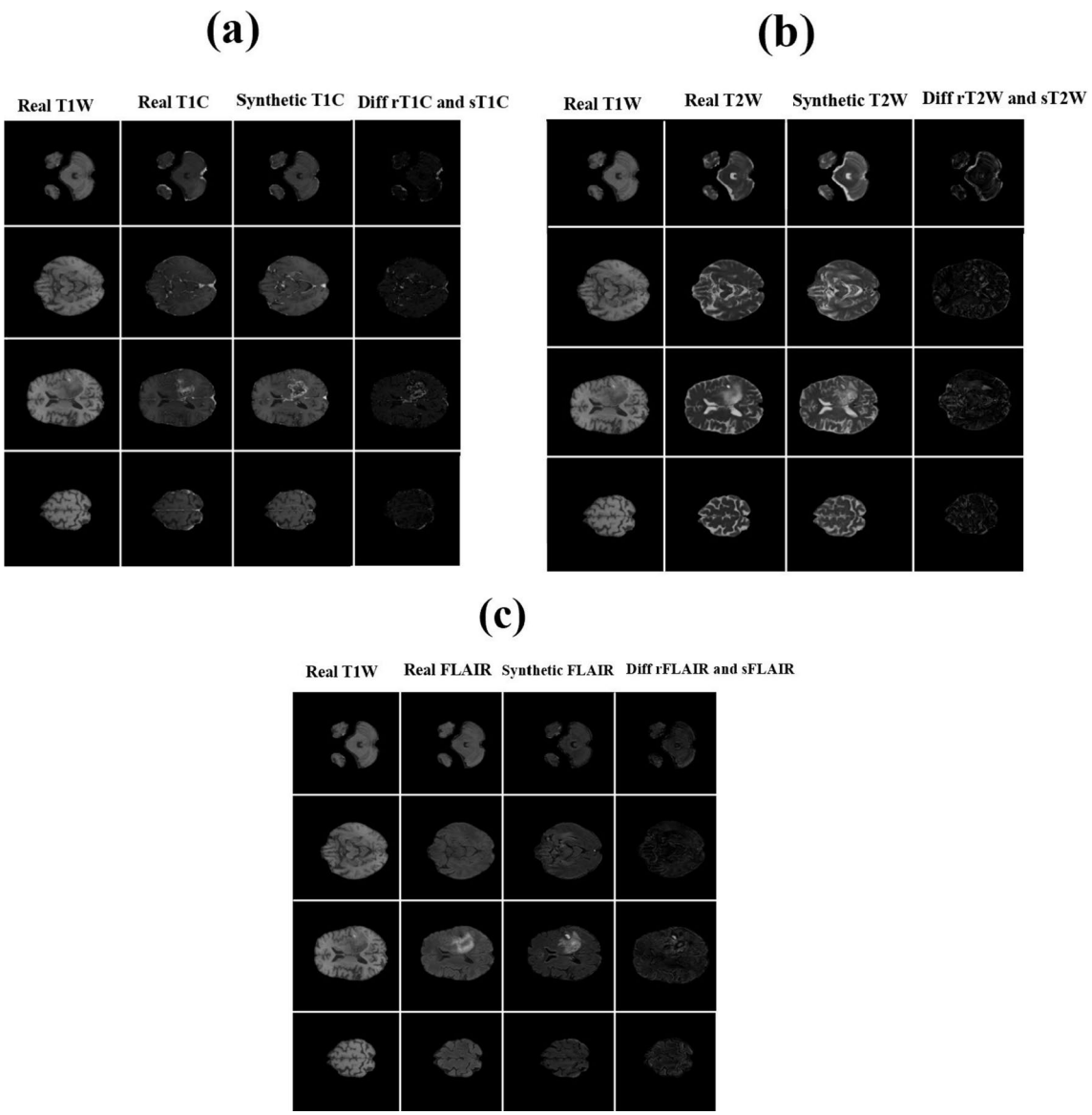

Fig. 5 Visual comparison for Generating T1c images from T1W images (**a**), generating T2W images from T1W images (**b**), and generating FLAIR images from T1W images

Furthermore, Xu et al. [37] proposed a bidirectional prediction method using multi-generative multi-adversarial nets (Bi-MGAN) for estimating desired modalities from acquired modalities. Their study aimed to predict desired modalities from acquired modalities without the need for real acquisition, reducing costs and improving throughput. The experimental outcomes indicate that Bi-MGAN successfully maintains the pathological features and anatomical structure of the generated images. It exhibits substantial improvements when applied to paired datasets and delivers competitive results even when dealing with unpaired datasets. Specifically, it achieves an average increase of 57.1% in SSIM, 47.1% in FSIM, and 50.0% in MSIM when applied to the paired SPLP dataset. Furthermore, it achieves a 9.1% increase in SSIM, 3.6% in FSIM, and 9.6% in MSIM when dealing with the unpaired Brain dataset. While their study focused on bidirectional prediction, our study concentrated on synthesizing multi-contrast MRI images. Both studies showcase the versatility of deep learning algorithms in medical imaging, but with different applications and objectives. Additionally, Fei et al. [18] developed a deep learning-based multi-modal computing model for MRI synthesis with a feature disentanglement strategy. Their goal was

to predict target MRI sequences with high accuracy, providing more information for clinical diagnosis. Although their study focuses on predicting target sequences rather than multi-contrast synthesis, both studies emphasize the importance of deep learning in improving the quality and usefulness of MRI exams. Finally, Dar et al. proposed a new approach for multi-contrast MRI synthesis based on conditional generative adversarial networks (GANs). Their approach aimed to preserve structural details and enhance synthesis performance. Both studies primarily focused on multi-contrast synthesis, and emphasize the benefits of GAN-based approaches in improving the quality and versatility of multi-contrast MRI exams.

In summary, our study successfully utilized the 3D Dual CycleGAN algorithm to synthesize T1c, T2W, and FLAIR images from T1W inputs, contributing to the improved identification of glioma tumors. Although the objectives and methodologies varied among the compared studies, they all underscored the effectiveness of deep learning algorithms in enhancing medical image synthesis. The findings from these studies collectively demonstrate the potential of deep learning in the field of medical imaging, paving the way for further advancements and improvements in diagnostic accuracy and patient care.

Limitations, challenges, and areas for further investigation in future research

In conclusion, while our study shows promise in MR image synthesis, limitations exist. Generalizability beyond the BraTS 2021 dataset is uncertain. Subjective evaluation methods are needed for clinical relevance. Our focus on glioma tumors limits applicability to other conditions. Reliance on T1W inputs may introduce biases. Overcoming these limitations requires diverse datasets and comprehensive evaluation to enhance reliability in medical imaging. Despite the promising results obtained from the implementation of the proposed methods, there are several limitations to acknowledge in our study. Firstly, our study heavily relied on the MRI data sourced from the Multi-modal BraTS 2021 dataset. While this dataset provided a substantial number of MR volumes with dimensions of $240 \times 240 \times 155$, it is essential to note that the generalizability of our findings may be limited to this specific dataset. The diversity and variability of brain tumor cases across different datasets and populations might introduce uncertainties and potential biases in the performance of our model when applied to other datasets. Secondly, our study focused on the synthesis of T1c, T2W, and FLAIR images from T1W inputs using the 3D Dual-CycleGAN model. Although we achieved remarkable results, the evaluation was primarily conducted using quantitative metrics such as MAE, RMSE, SSIM, PCC, and PSNR. While these metrics provide valuable insights into the performance of the model, they do not encompass the full spectrum of image quality assessment. Future studies should consider incorporating more comprehensive subjective evaluation methods, such as clinical validation, to ensure the clinical relevance and reliability of the synthesized images. Furthermore, it is important to note that our study focused on the synthesis of T1c, T2W, and FLAIR images and their application in glioma tumor identification. The evaluation and generalizability of the proposed methods to other types of tumors or medical conditions were not extensively explored. The effectiveness and applicability of the Dual-CycleGAN model in different clinical scenarios warrant further investigation and validation.

Lastly, while our study demonstrated the effectiveness of the proposed methods in synthesizing multi-contrast MRI images, it is crucial to recognize that the synthetic images are generated based on the information present in the T1W inputs. Any limitations, artifacts, or biases in the T1W images can potentially propagate to the synthesized images. Therefore, the quality and reliability of the generated images heavily rely on the accuracy and consistency of the T1W inputs. In conclusion, while our study showcased promising results and advancements in the field of MR image synthesis, it is important to consider the limitations outlined above. Future research should address these limitations by incorporating diverse datasets, comprehensive evaluation methods, optimized training procedures, and further exploration of the model's generalizability to different clinical contexts. By doing so, we can enhance the reliability, applicability, and clinical utility of our proposed methods in the field of medical imaging and tumor identification.

Conclusions

In this research endeavor, we introduced the innovative Dual-CycleGAN model as a solution to the challenge of cross-sequence synthesis of 3D brain MR images. Our methodology encompassed a comprehensive objective function comprising six distinct loss terms. Through meticulous ablation analysis, we systematically evaluated the effectiveness and relative significance of each loss term. The integration of these diverse loss functions resulted in significant improvements in performance, as each term demonstrated unique strengths and weaknesses. Notably, the incorporation of adversarial and dual cycle-consistency loss functions played a pivotal role in enhancing the accuracy of synthesized images, particularly in capturing intricate structural details across various contrasts. By employing our proposed method to generate T1c, T2W, and FLAIR images from T1W inputs, we presented compelling evidence of its superior performance compared to other existing state-of-the-art

approaches. Our findings unequivocally establish the suitability and efficacy of our approach for cross-sequence image synthesis.

Appendix

Mean absolute error (MAE)

The mean absolute error (MAE) is a widely used metric for evaluating the performance of regression models or forecasting techniques. It measures the average magnitude of the absolute differences between predicted values and actual values. The formula for MAE is given by::

$$MAE = \frac{1}{n}\sum_{i=1}^{n}\left|y_i - \widehat{y_i}\right|$$

where n is the number of observations, y_i is the actual value of the ith observation, and $\widehat{y_i}$ is the predicted value of the ith observation.

Percent mean absolute error (PMAE)

The percent mean absolute error (PMAE) is a variation of the mean absolute error (MAE) that expresses the error as a percentage of the actual values. It is particularly useful when the scale of the target variable is important or when comparing errors across different datasets with varying scales. The formula for PMAE is:

$$PMAE = \frac{100}{n}\sum_{i=1}^{n}\left|\frac{y_i - \widehat{y_i}}{y_i}\right|$$

where n, y_i, and $\widehat{y_i}$ have the same meanings as in the MAE formula.

Root mean squared error (RMSE)

The root mean squared error (RMSE) is another widely used metric for evaluating regression models or forecasting techniques. It measures the square root of the average squared differences between the predicted values and the actual values. The formula for RMSE is:

$$RMSE = \sqrt{\frac{1}{n}\sum_{i=1}^{n}\left(y_i - \widehat{y_i}\right)^2}$$

where n, y_i, and $\widehat{y_i}$ have the same meanings as in the MAE formula.

Pearson correlation coefficient (PCC)

The Pearson correlation coefficient (PCC) measures the linear correlation between two variables. It quantifies the strength and direction of the linear relationship between the predicted values and the actual values. The formula for PCC is:

$$PCC = \frac{\sum_{i=1}^{n}\left(y_i - \bar{y}\right)\left(\widehat{y_i} - \bar{\widehat{y}}\right)}{\sqrt{\frac{1}{n}\sum_{i=1}^{n}\left(y_i - \bar{y}\right)^2}\sqrt{\frac{1}{n}\sum_{i=1}^{n}\left(\widehat{y_i} - \bar{\widehat{y}}\right)^2}}$$

where n is the number of observations, y_i is the actual value of the ith observation, $\widehat{y_i}$ is the predicted value of the ith observation, $\bar{y}$ is the mean of the actual values, and $\bar{\widehat{y}}$ is the mean of the predicted values.

Peak-signal-to-noise ratio (PSNR)

The peak-signal-to-noise ratio (PSNR) is a metric commonly used in image and video processing to evaluate the quality of reconstructed or compressed images or videos. It measures the ratio between the maximum possible signal value and the distortion or noise introduced by the compression or reconstruction process. The formula for PSNR is:

$$PSNR = 10\log_{10}\left(\frac{MAX_I^2}{MSE}\right)$$

where MAX is the maximum possible pixel value of the image (e.g., 255 for an 8-bit grayscale image), and MSE is the Mean Squared Error between the original image and the reconstructed or compressed image.

The mean squared error (MSE) is defined as:

$$MSE = \frac{1}{mn}\sum_{i=0}^{m-1}\sum_{j=0}^{n-1}\left[I(i,j) - K(i,j)\right]^2$$

where m and n are the dimensions of the image (height and width, respectively), $I(i,j)$ is the pixel value at coordinates (i,j) in the original image and $K(i,j)$ is the pixel value at coordinates (i,j) in the reconstructed or compressed image. The MSE calculates the average squared difference between the pixel values of the original and reconstructed/compressed images. A lower MSE value indicates a smaller difference between the two images, and consequently, a higher PSNR value, which implies better image quality.

Structural similarity index measure (SSIM)

The structural similarity index measure (SSIM) is another metric used in image and video processing to evaluate the quality of reconstructed or compressed images or videos. It measures the perceived similarity between two images by considering their structural information, luminance, and contrast. The formula for SSIM is:

$$SSIM(x,y) = \frac{\left(2\mu_x\mu_y + C_1\right)\left(2\sigma_{xy} + C_2\right)}{\left(\mu_x^2 + \mu_y^2 + C_1\right)\left(\sigma_x^2 + \sigma_y^2 + C_2\right)}$$

where x and y are the original and reconstructed or compressed images, respectively, μ_x and μ_y are the mean values of x and y, σ_x and σ_y are the standard deviations of x and y, σ_{xy} is the covariance between x and y, and C_1 and C_2 are small constants to avoid division by zero.

Abbreviations

MRI	Magnetic resonance imaging
CT	Computed tomography
B-scan	B ultrasonic
PET	Positron emission topography
T1W	T1-weighted
T2W	T2-weighted
T1c	T1-with-contrast-enhanced
FLAIR	T2-fluid-attenuated inversion recovery
CNN	Convolutional neural networks
GAN	Generative adversarial network
BraTS	Brain tumour segmentation challenge
ET	Enhancingtumor
NET	Non-enhancingtumor
NCR	Necrotic tumor
ED	Peritumoral edema
LGAN	The adversarial loss
MAE	Mean absolute error
PMAE	Percent mean absolute error
RMSE	Root mean squared error
PCC	Pearson correlation coefficient
PSNR	Peak-signal-to-noise ratio
SSIM	Structural similarity index measure

Acknowledgements
The authors would like to extend their sincere gratitude to Ahvaz Jundishapur University of Medical Sciences for their financial support and technical assistance.

Author contributions
SMR and AM are responsible for the study conception, design, data acquisition and analysis, drafting, and finalizing the manuscript. HS, SJN, MAK, MN, and MT contributed in the data acquisition and analysis and also the drafting and approval of the final manuscript. All authors read and approved the final manuscript.

Funding
Not applicable.

Availability of data and materials
Data and code about the results of this study will publicly share at: https://github.com/MASOUD-AJUMS/Enhancing-3D-Multi-Contrast-MRI-Synthesis-with-the-3D-Dual-CycleGAN-Model Data: https://www.synapse.org/#!Synapse:syn51156910/wiki/622345.

Declarations

Ethics approval and consent to participate
Not applicable.

Consent for publication
Not applicable.

Competing interests
The authors declare that they have no conflict of interest.

Received: 15 February 2024 Accepted: 30 May 2024
Published online: 11 June 2024

References

1. Tirotta I, Dichiarante V, Pigliacelli C, Cavallo G, Terraneo G, Bombelli FB et al (2015) 19F magnetic resonance imaging (MRI): from design of materials to clinical applications. Chem Rev 115:1106–1129
2. Katti G, Ara SA, Shireen A (2011) Magnetic resonance imaging (MRI)—a review. Int J Dent Clin 3:65–70
3. Khanfari H, Mehranfar S, Cheki M, Mohammadi Sadr M, Moniri S, Heydarheydari S, Rezaeijo SM (2023) Exploring the efficacy of multi-flavored feature extraction with radiomics and deep features for prostate cancer grading on mpMRI. BMC Med Imaging 23(1):195
4. Salmanpour MR, Hosseinzadeh M, Akbari A, Borazjani K, Mojallal K, Askari D, Hajianfar G, Rezaeijo SM, Ghaemi MM, Nabizadeh AH, Rahmim A (2022) Prediction of TNM stage in head and neck cancer using hybrid machine learning systems and radiomics features. In: Medical imaging 2022: computer-aided diagnosis, vol 12033. SPIE, pp 662–667
5. Enevoldsen LH, Menashi CAK, Andersen UB, Jensen LT, Henriksen OM (2013) Effects of acquisition time and reconstruction algorithm on image quality, quantitative parameters, and clinical interpretation of myocardial perfusion imaging. J Nucl Cardiol 20:1086–1092
6. Edelman RR, Wielopolski P, Schmitt F (1994) Echo-planar MR imaging. Radiology 192:600–612
7. Wang T, Lei Y, Fu Y, Wynne JF, Curran WJ, Liu T et al (2021) A review on medical imaging synthesis using deep learning and its clinical applications. J Appl Clin Med Phys 22:11–36
8. Nie D, Trullo R, Lian J, Wang L, Petitjean C, Ruan S et al (2018) Medical image synthesis with deep convolutional adversarial networks. IEEE Trans Biomed Eng 65:2720–2730
9. Nie D, Trullo R, Lian J, Petitjean C, Ruan S, Wang Q et al (2017) Medical image synthesis with context-aware generative adversarial networks. In: International conference on medical image computing and computer-assisted intervention. Springer, pp 417–25
10. Zhang Q, Wang H, Lu H, Won D, Yoon SW (2018) Medical image synthesis with generative adversarial networks for tissue recognition. In: 2018 IEEE international conference on healthcare informatics (ICHI). IEEE, pp 199–207
11. Yang J, Li X-X, Liu F, Nie D, Lio P, Qi H et al (2021) Fast T2w/FLAIR MRI acquisition by optimal sampling of information complementary to pre-acquired T1w MRI. ArXiv Preprint ArXiv:211106400
12. Pan K, Cheng P, Huang Z, Lin L, Tang X (2022) Transformer-based T2-weighted MRI synthesis from T1-weighted images. In: 2022 44th annual international conference of the IEEE engineering in medicine & biology society (EMBC). IEEE, pp 5062–5065
13. Kwon HY (2020) Generating synthetic gadolinium-enhanced t1-weighted (gd-t1w) mri
14. Moya-Sáez E, Peña-Nogales Ó, de Luis-García R, Alberola-López C (2021) A deep learning approach for synthetic MRI based on two routine sequences and training with synthetic data. Comput Methods Programs Biomed 210:106371
15. Fatan M, Hosseinzadeh M, Askari D, Sheikhi H, Rezaeijo SM, Salmanpour MR (2021) Fusion-based head and neck tumor segmentation and survival prediction using robust deep learning techniques and advanced hybrid machine learning systems. In: 3D head and neck tumor segmentation in PET/CT challenge 2021 Sep 27. Springer, Cham, pp 211–223
16. Zhou T, Fu H, Chen G, Shen J, Shao L (2020) Hi-net: hybrid-fusion network for multi-modal MR image synthesis. IEEE Trans Med Imaging 39:2772–2781
17. Zhan B, Li D, Wu X, Zhou J, Wang Y (2021) Multi-modal MRI image synthesis via GAN with multi-scale gate mergence. IEEE J Biomed Health Inform 26:17–26
18. Fei Y, Zhan B, Hong M, Wu X, Zhou J, Wang Y (2021) Deep learning-based multi-modal computing with feature disentanglement for MRI image synthesis. Med Phys 48:3778–3789
19. Joyce T, Chartsias A, Tsaftaris SA (2017) Robust multi-modal MR image synthesis. In: Medical image computing and computer assisted intervention—MICCAI 2017: 20th international conference, Quebec City, QC, Canada, September 11–13, 2017, proceedings, Part III 20. Springer, pp 347–55
20. Chartsias A, Joyce T, Dharmakumar R, Tsaftaris SA (2017) Adversarial image synthesis for unpaired multi-modal cardiac data. In: Simulation and synthesis in medical imaging: second international workshop,

SASHIMI 2017, held in conjunction with MICCAI 2017, Québec City, QC, Canada, September 10, 2017, proceedings 2. Springer, pp 3–13
21. Xie G, Wang J, Huang Y, Zheng Y, Zheng F, Song J et al (2022) FedMed-GAN: federated multi-modal unsupervised brain image synthesis. ArXiv Preprint ArXiv:220108953
22. Liu M-Y, Breuel T, Kautz J (2017) Unsupervised image-to-image translation networks. Adv Neural Inf Process Syst 30:21
23. Koike Y, Anetai Y, Takegawa H, Ohira S, Nakamura S, Tanigawa N (2020) Deep learning-based metal artifact reduction using cycle-consistent adversarial network for intensity-modulated head and neck radiation therapy treatment planning. Physica Med 78:8–14
24. Tahri S, Barateau A, Cadin C, Chourak H, Ribault S, Nozahic F et al (2022) A high-performance method of deep learning for prostate MR-only radiotherapy planning using an optimized Pix2Pix architecture. Physica Med 103:108–118
25. Cusumano D, Boldrini L, Dhont J, Fiorino C, Green O, Güngör G et al (2021) Artificial intelligence in magnetic resonance guided radiotherapy: medical and physical considerations on state of art and future perspectives. Physica Med 85:175–191
26. Altini N, Prencipe B, Cascarano GD, Brunetti A, Brunetti G, Triggiani V et al (2022) Liver, kidney and spleen segmentation from CT scans and MRI with deep learning: a survey. Neurocomputing 490:30–53
27. Dou H, Chen C, Hu X, Jia L, Peng S (2020) Asymmetric CycleGAN for image-to-image translations with uneven complexities. Neurocomputing 415:114–122
28. Luo Y, Nie D, Zhan B, Li Z, Wu X, Zhou J et al (2021) Edge-preserving MRI image synthesis via adversarial network with iterative multi-scale fusion. Neurocomputing 452:63–77
29. Masoud Rezaeijo S, Chegeni N, Baghaei Naeini F, Makris D, Bakas S (2023) Within-modality synthesis and novel radiomic evaluation of brain MRI scans. Cancers 15:3565
30. Isola P, Zhu J-Y, Zhou T, Efros AA (2017) Image-to-image translation with conditional adversarial networks. In: Proceedings of the IEEE conference on computer vision and pattern recognition, pp 1125–1134
31. Bakas S, Akbari H, Sotiras A, Bilello M, Rozycki M, Kirby JS et al (2017) Advancing the cancer genome atlas glioma MRI collections with expert segmentation labels and radiomic features. Sci Data 4:1–13
32. Bakas S (2017) Segmentation labels and radiomic features for the pre-operative scans of the TCGA-GBM collection
33. Lee RS, Gimenez F, Hoogi A, Rubin D (2016) Curated breast imaging subset of DDSM. Cancer Imaging Arch 8:2016
34. Menze B, Jakab A, Bauer S, Kalpathy-Cramer J, Farahani K, Kirby J (2014) The multimodal brain tumor image segmentation benchmark (brats). IEEE Trans Med Imaging 34:1–32
35. Xie H, Lei Y, Wang T, Roper J, Dhabaan AH, Bradley JD et al (2022) Synthesizing high-resolution magnetic resonance imaging using parallel cycle-consistent generative adversarial networks for fast magnetic resonance imaging. Med Phys 49:357–369
36. Xie H, Lei Y, Wang T, Roper J, Axente M, Bradley JD et al (2022) Magnetic resonance imaging contrast enhancement synthesis using cascade networks with local supervision. Med Phys 49:3278–3287
37. Xu L, Zhang H, Song L, Lei Y (2022) Bi-MGAN: bidirectional T1-to-T2 MRI images prediction using multi-generative multi-adversarial nets. Biomed Signal Process Control 78:103994

Publisher's Note